CrossMark

Investigation of optical and electrical properties of erbium-doped TiO$_2$ thin films for photodetector applications

Sanjib Mondal[1,9] · Anupam Ghosh[1] · M. Rizzo Piton[2] · Joaquim P. Gomes[3,10] · Jorlandio F. Felix[3,4] · Y. Galvão Gobato[2] · H. V. Avanço Galeti[5] · B. Choudhuri[6] · S. M. M. Dhar Dwivedi[1] · M. Henini[7,8] · Aniruddha Mondal[1]

Abstract

We have investigated the electrical and optical properties of erbium (Er^{3+}) doped TiO$_2$ thin films (Er:TiO$_2$ TFs) grown by sol–gel technique on glass and silicon substrates. The samples were characterized by field emission gun–scanning electron microscopes (FEG–SEM), energy dispersive X-ray spectroscopy (EDX), atomic force microscopy (AFM), X-ray diffraction (XRD), photoluminescence (PL) and current–voltage measurement techniques. FEG–SEM and AFM images showed the morphological change in the structure of Er:TiO$_2$ TFs and EDX analysis confirmed the Er^{3+} doped into TiO$_2$ lattice. Broad PL emissions in visible and infrared regions were observed in undoped TiO$_2$ samples and associated to different mechanisms due to the anatase and rutile phases. PL spectra revealed sharp peaks at 525 nm, 565 nm, 667 nm and 1.54 µm which are related to Er^{3+} emissions in Er:TiO$_2$ samples. The undoped TiO$_2$ and Er:TiO$_2$ TFs based UV-photodetectors were fabricated, and various device parameters were investigated. The doped devices exhibit high photoresponse upon illuminating 350 nm UV light at 2 V bias with faster response time compared to undoped device.

1 Introduction

TiO$_2$ is an attractive material due to its efficient photo activity, high chemical stability, nontoxicity and cost-effectiveness [1–3]. It has been extensively used for making sensors [4, 5], ultraviolet (UV) detectors [6, 7], low cost solar cells [8] and for applications in photo-electrochemical water splitting [2]. The technological interests of rare earth luminescence are in the field of telecommunications [9], flat panel displays [10], laser materials [11], data storage [12], radiation detection [13], medical applications [14] etc. Several attempts have been made to enhance the

photo activity of TiO$_2$ into the visible region by doping it with lanthanide materials like erbium (Er), europium (Eu), terbium (Tb) and cerium (Ce) [15–17]. Particularly, incorporation of Er^{3+} ions into TiO$_2$ semiconductors draws special attention due to some interesting features associated with its unique optical and electrical characteristics. The sharp photoemission from Er^{3+} doped TiO$_2$ at 1.54 µm due to intra 4f-shell transition of Er^{3+} ions, which has been reported by several groups [9, 11, 18], is important for telecommunication applications [18]. In addition, the interaction between the local electric field of the host and the 4f electrons is weak. Therefore, the local

✉ Aniruddha Mondal
aniruddhamo@gmail.com

1 Department of Physics, National Institute of Technology Durgapur, Durgapur 713209, India

2 Departamento de Física, Universidade Federal de São Carlos (UFSCar), São Carlos, SP 13565-905, Brazil

3 Department of Physics, Universidade Federal de Viçosa-UFV, Viçosa, Brazil

4 Institute of Physics, Universidade de Brasília, Brasília, DF 70910-900, Brazil

5 Departamento de Engenharia Elétrica, Universidade Federal de São Carlos(UFSCar), São Carlos, SP 13565-905, Brazil

6 Department of Electronics and Communication Engineering, National Institute of Technology Nagaland, Dimapur 797103, India

7 School of Physics and Astronomy, University of Nottingham, Nottingham NG7 2RD, UK

8 UNESCO-UNISA Africa Chair in Nanoscience's/Nanotechnology Laboratories, College of Graduate Studies, University of South Africa (UNISA), Muckleneuk Ridge, P O Box 392, Pretoria, South Africa

9 Suri Vidyasagar College, Suri, Birbhum 731101, India

10 IFNMG - instituto Federal do Norte de Minas Gerais, Januaria, MG, Brazil

host structure around Er^{3+} would result in minor splitting of the free-ion energy levels, $^{2S+1}L_J$, into multiplets. This splitting is usually called crystal-field (CF) splitting or Stark splitting, and the number of CF sublevels is determined by the symmetry of the surrounding crystal host, such that a reduction in the symmetry around the lanthanide ions will introduce a higher number of sub-levels. It was previously observed that in Er^{3+} doped TiO_2 materials the crystallinity of TiO_2 affects considerably the light emission from Er^{3+}, and the CF splitting of the energy levels of Er^{3+} ions. Particularly, this emission from a polycrystalline host depends on anatase or rutile phases that were observed in the $Er:TiO_2$ samples. Different methods such as sputtering [19], electron beam evaporation [20], hydrothermal [21], chemical bath deposition [22] spray pyrolysis [23] and sol–gel [24] have been demonstrated for the synthesis of TiO_2 nanostructures. Among these methods, sol–gel spin-on has the advantages of being relatively easy preparation technique, employing less sophisticated instruments and having short operation time to synthesize TFs. In recent years a lot of attempts have been made to improve the properties of TiO_2 based UV photodetectors. For example, Xing et al. reported that the TiO_2 nanocrystalline films photodetector exhibited a maximum photoresponse of 3.63 A/W at 310 nm [25]. Lv et al. prepared TiO_2 nanocrystalline film UV photodetectors with responsivity of 31.7 A/W at 5 V bias with response rise and fall times of 550 ms and 380 ms, respectively [26]. Selman et al. reported rutile TiO_2 nanorods based devices with responsivity and internal gain of 460 mA/W and 4.79, respectively, upon illuminating UV pulsed (325 nm) at 5 V [7]. In a recent report Patel et al. demonstrated that they fabricated high responsivity (2.023 A/W) with faster rise time (0.14 ms) nanocrystalline TiO_2 thin film based UV detector at 1 V reverse bias [27]. Xiang reported work on a commercial TiO_2 based UV photodiode (TW30SX photodiode from sglux SolGel Technologies GmbH) which had a maximum spectral sensitivity of 0.021 A/W (active area of 4.18 mm^2) at 1 V reverse bias [28]. However, the photoresponse value of the detector can be different under different applied biasing conditions. In addition, due to the complicated and costly fabrication process [29] of TiO_2 semiconductor based photodetectors their use is not suitable in large scale production.

In this article, we report an enhancement in photoresponse due to Er^{3+} ions incorporation into the TiO_2 host by using easy and cost effectiveness chemical synthesis method. We have shown that responsivity of doped UV photodetector ($Er:TiO_2$ TF) significantly increases as compared to undoped TiO_2 upon illuminating 350 nm under applied bias of 2 V. The doped device also exhibits faster response time than that of undoped device. The

Er^{3+}-doped TiO_2 lattice has been confirmed by optical and electrical characterization techniques.

2 Experimental details

Undoped and Er-doped TiO_2 TFs were deposited on glass and p-type silicon (Si) substrates using sol–gel technique followed by spin coating. Titanium isopropoxide (TTIP) was used as a precursor (Sigma-Aldrich, purity $\geq 97\%$) of TiO_2 material. Erbium oxide nanopowder (Er_2O_3, Sigma-Aldrich, purity $\geq 99.9\%$) was used to dope TiO_2 TFs with Er^{3+} ions. To produce a proper solution for spin coating of undoped TiO_2 TFs, firstly, a homogeneous solution was prepared by mixing 10 ml ethanol (purity $\geq 99.9\%$, analytic reagent, Changshu Yanguan Chemical) and 2 ml glacial acetic acid (purity $\geq 99.8\%$, Merck) under ultra-sonication for 10 min duration. Then, 2 ml TTIP was added to the solution. The final solution was ultra-sonicated for 30 min and was left for 48 h of ageing in a test tube to form the gel. To make $Er:TiO_2$ solutions, 0.04 g and 0.06 g Er_2O_3 nanopowder were mixed into two other undoped TiO_2 solutions prepared by same compositions as mentioned before. To dissolve Er_2O_3 nano powder, 2 ml hydrochloric acid (HCl) was mixed into the solution which has 0.04 g Er_2O_3 and 3 ml HCl was mixed into the other solution which has 0.06 g Er_2O_3. Finally the solutions were ultra-sonicated for 30 min and were aged for a period of 48 h to form the gel. The glass and (100) p-type Si substrates (MTI, USA) were rinsed well with de-ionized water and finally cleaned with acetone followed by Radio Corporation of America and HF dip cleaning for Si substrates. The TFs were deposited by spin coating (spin NXG-P1, apexicindia) technique with substrate rotation speed of ~ 3000 rpm for 1 min on glass substrates and 4000 rpm for 1.5 min on Si substrates. The films were open-air annealed at 200 °C for 2 min in a muffle furnace. To obtain uniform TFs, the entire coating and annealing process were repeated three times with final annealing at 450 °C for 1.5 h in air atmosphere. Gold (Au) was evaporated through a shadow mask with holes of a diameter of 1 mm using a thermal evaporator (Pro-Vak, Pune) to form Schottky contact on the TFs.

The surface and structural morphology of the TFs was characterized by using field emission gun–scanning electron microscopes (JEOL JSM-7600F FEG–SEM), energy dispersive X-ray spectroscopy (EDX), atomic force microscopy (AFM: NT-MDT-INTEGRA) and X-ray diffraction (XRD: Bruker D8 Discover Diffractometer) using Cu Kα radiation ($\lambda = 1.5418$ Å). The room temperature diffraction pattern was obtained at diffraction angles between 20° and 80° with geometry 2θ. Temperature-dependent photoluminescence (PL) measurements were performed using a 325 nm Kimmon He–Cd laser and a closed cycle Janis cryostat. The PL spectra were obtained by using Triax Horiba spectrometer

coupled with GaAs photomultiplier for visible emission or liquid-N_2 cooled Ge detector for near-infrared emission. The current–voltage (I–V) characteristics and photo-response of the Schottky contact based devices were measured using a Keithley 2401 source meter with a 300 W xenon arc lamp and a monochromator (Sciencetech, Canada) connected in open beam configuration.

3 Results and discussions

3.1 FEG–SEM with EDX and AFM analysis

The surface morphology of undoped and Er-doped TiO_2 TFs are shown in (Fig. 1a, c, e). The top view of FEG–SEM image of the undoped sample shows that the Ti nanoparticles (NP) are evenly distributed over the cracked surface. The images of doped TFs show that the surface become gradually smooth and grain structure lost with an increase of Er^{3+} ions doping concentration. The particle size histogram (inset), which are plotted based on FEG–SEM images show that the samples consist of different size NPs ranging from 10 to 40 nm. The average particles size is 27 nm for undoped TF and gradually reduces as the dopant level increases to 22 nm for 0.75 at.% Er and 16 nm for 0.98 at.% Er doped into TiO_2 lattice as confirmed by EDX analysis. This can be attributed to the increase of Er^{3+} ions in the solution, the electrostatic interaction between the particles becomes larger, which increases the probability of gathering more ions together. This demonstrates that the Er^{3+} doping affects the morphology of pure TiO_2 material and the size of NPs reduces due to the strong influence of doping ions. Besides that Er^{3+} ions can react strongly with TiO_2 host in solid state phase and changes the thin film structure. Similar reaction mechanism of Er^{3+} ions with ZnO and In_2O_3 host have been reported by Miao, Ghosh et al. [30, 31]. The EDX spectra (Fig. 1b) shows the presence of titanium (Ti), and oxygen (O_2) elements in the undoped sample and the element erbium (Er) atoms along with Ti and O atoms are observed in all the doped TFs, showing that definite doping of Er^{3+} ions into TiO_2 (Fig. 1d, f). The atomic fraction of Er^{3+} ions in the doped films are estimated to be 0.75 at.% and 0.98 at.% for the 0.04 g Er_2O_3 and 0.06 g Er_2O_3 containing samples, respectively. The chemical mapping of FEG–SEM images (inset of Fig. 1b, d, f) of the samples, which show the presence of Ti (green color), O_2 (red color) and Er (blue color).

The surface topography, roughness and particle size of undoped and doped TFs are also examined using AFM images which are shown in Fig. 2. The average peak height and root mean square roughness (S_q) of undoped film surface are 6.09 nm and 1.79 nm, respectively. Whereas for the doped film surfaces these are 2.17 nm and 0.53 nm (0.75 at.% Er) and 1.74 nm and 0.44 nm (0.98 at.% Er),

respectively which indicate that the surfaces are becoming flatten and smooth with increasing doping concentration. The particle sizes are also estimated from 3D view of AFM images which are about 30 nm for undoped sample and reduce as doping increases. The thickness of thin films are about 150 nm as measured from the cross-sectional views of FEG–SEM image of undoped sample shown in the inset of Fig. 1a.

3.2 XRD analysis

The θ/2θ XRD patterns of the undoped TiO_2 and Er:TiO_2 TFs are shown in Fig. 3a. As can be seen from this figure, all detectable diffraction peaks from these samples have the signature of single-phase anatase TiO_2 at room temperature. The diffraction peaks occur around 2θ = 25.3°, 48.1°, and 61.9° for undoped and doped TFs, which correspond to the (101), (200), and (213) planes of body-centered tetragonal anatase TiO_2 crystal structure, respectively. All the peaks of TiO_2 are in good agreement with the standard spectrum (JCPDS Card no: 84-1286). However, using a grazing incidence with the ω angle equal to 1°, rutile (JCPDS Card no. 21-1276) peaks are also observed at 2θ values of 54.2° and 56.3°, which correspond to crystal planes of (211) and (220), as shown in Fig. 3b. This result shows that the anatase phase is the predominant phase. Our XRD results are also in agreement with the PL results, as will be discussed below. There are two another diffraction peaks occurring at 2θ = 33° and 69.2° which can be attributed to Si (100) substrate. The crystallite sizes were calculated from the full width at half maximum (FWHM) of (101) anatase peak using the Scherrer formula [32] (Eq. 1):

$$D_{hkl} = \frac{0.9\lambda}{\beta cos\theta} \tag{1}$$

where D_{hkl} denotes the crystallite size, λ = 0.154 nm is the X-ray wavelength of Cu Kα radiation, β is the FWHM in radian, and θ is the Bragg's angle. The calculated average crystallite sizes are ∼22 nm (for undoped TiO_2 TF), 20 nm (for 0.75 at.% Er doped TiO_2 TF) and 14 nm (for 0.98 at.% Er doped TiO_2 TF). These results show that the crystallite size decreases with the increase in concentration of Er^{3+} ions. Thus, it can be established that the larger amount of Er^{3+} ions doping causes widening of the width of the diffraction peaks and a reduction in the TiO_2 crystallite sizes. This decrease in crystallite size also may be due to the difference between the ionic radius of Er^{3+} (0.0881 nm) and Ti^{4+} (0.0605 nm). The incorporation of Er^{3+} ions into TiO_2 host matrix would create a tensile stress which restrict the growth of grain size and reduce the extent of crystallinity [33]. The
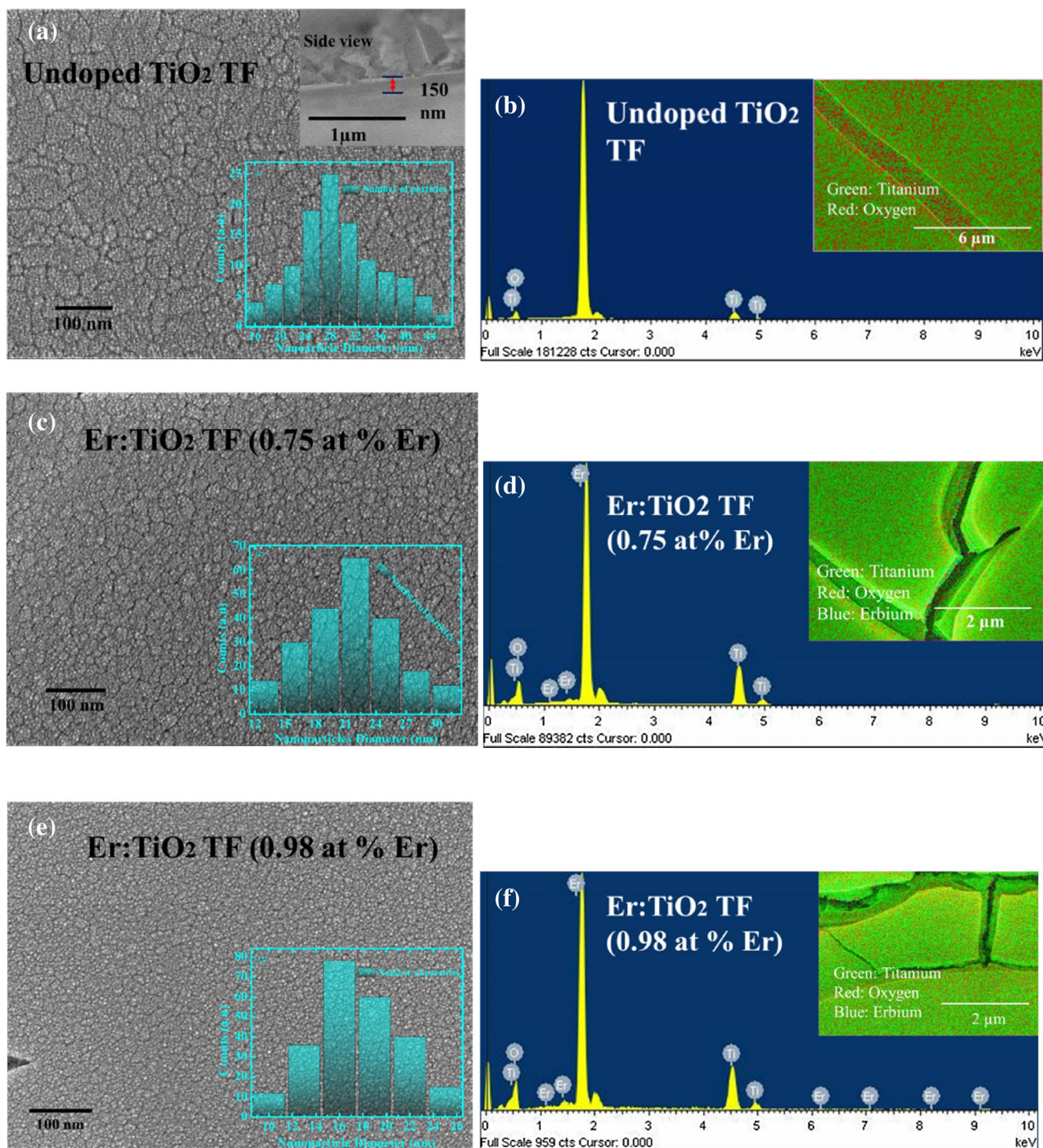
Fig. 1 FEG–SEM images: **a** top and cross-sectional view (inset) of undoped TiO_2 TF, **c, e** top view of 0.75 at.% Er and 0.98 at.% Er doped TiO_2 TF respectively. The insets correspond to the particle size histogram. **b, d, f** Show the EDX spectra and corresponding chemical mapping (inset) of undoped and doped samples. (Color figure online)

reduction of particle size with doping concentration has also been confirmed from FEG–SEM and AFM analysis, and the particle diameters are in close agreement as shown in Fig. 3c.
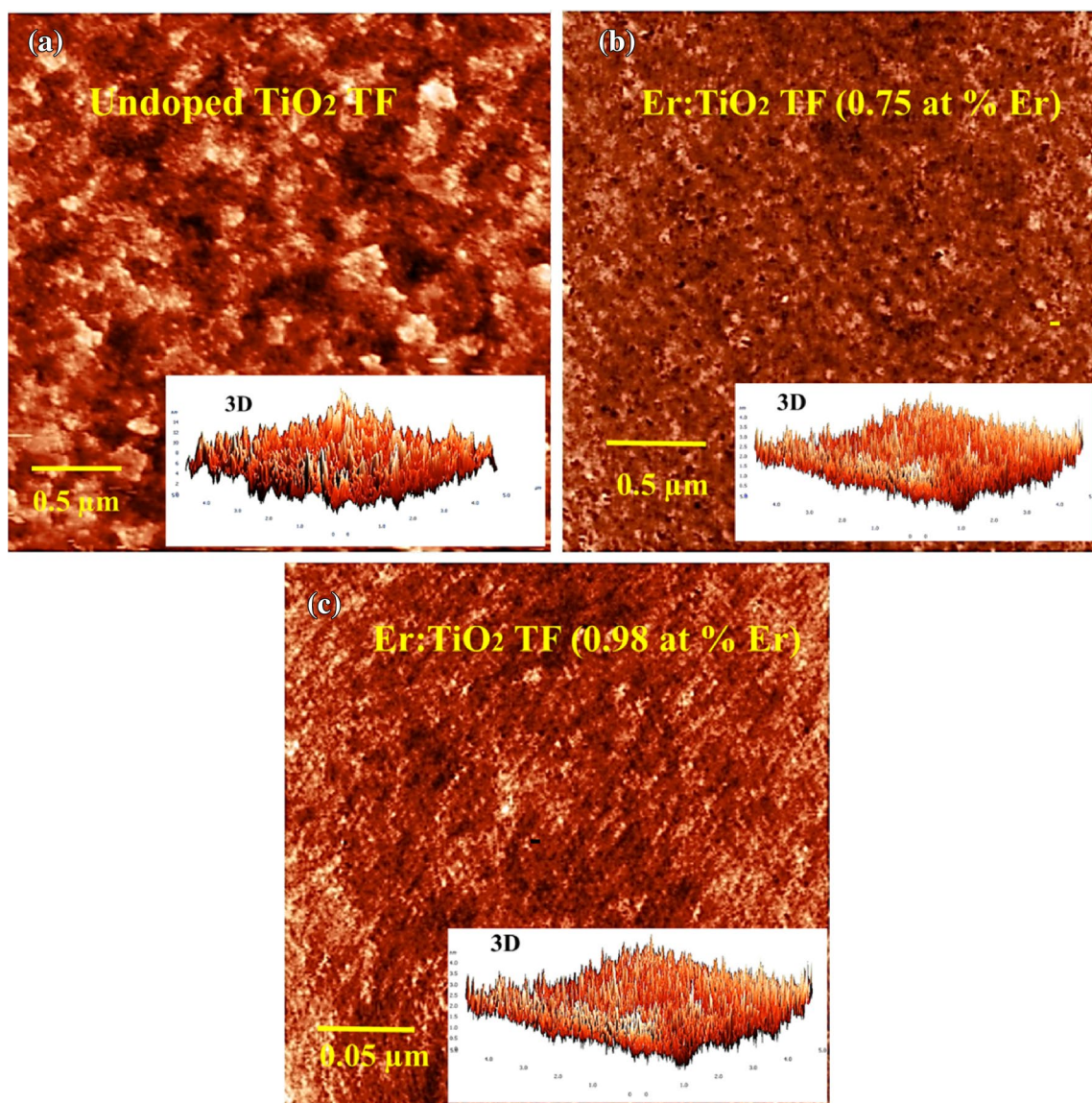
Fig. 2 AFM images: **a** undoped TiO$_2$ TF; **b** 0.75 at.% Er doped TiO$_2$; **c** 0.98 at.% Er doped TiO$_2$. The insets correspond the 3D views of AFM images

3.3 Photoluminescence

The PL spectra of the TiO$_2$ TFs deposited on glass were investigated as a function of temperature and laser power using a laser excitation wavelength of 325 nm. Figure 4 shows the typical temperature dependence of PL spectra for the undoped TiO$_2$ TF (reference sample) in visible (Fig. 4a) and infrared range (Fig. 4b). The PL spectra in Fig. 4 has been normalized by taking the maximum of the emission observed at around 403 nm and 1600 nm in Fig. 4a, b, respectively.

Three broad PL bands were observed around 403 nm (blue), 530 nm (green) and 750 nm (NIR). The nature of these bands for undoped samples will be discussed below.

It is well known that the PL spectrum of TiO$_2$ usually depends on the crystal phase (anatase, rutile or mixed phases) [34]. For the anatase phase, it was reported previously that the PL spectra show only green (~ 520 nm) and red (~ 620 nm) emissions. In general, the nature of these emissions is not well understood and there is not a well-established consensus on the processes and chemical nature of the states involved in the radiative transitions [34]. For example, the green band was previously associated to self-trapped excitons [35]. However, it was also reported that surface states of anatase TiO$_2$ phase could possibly contribute to the PL bands [36]. More recently, a detailed study of these emissions has evidenced that the green emission could be related to the following process:
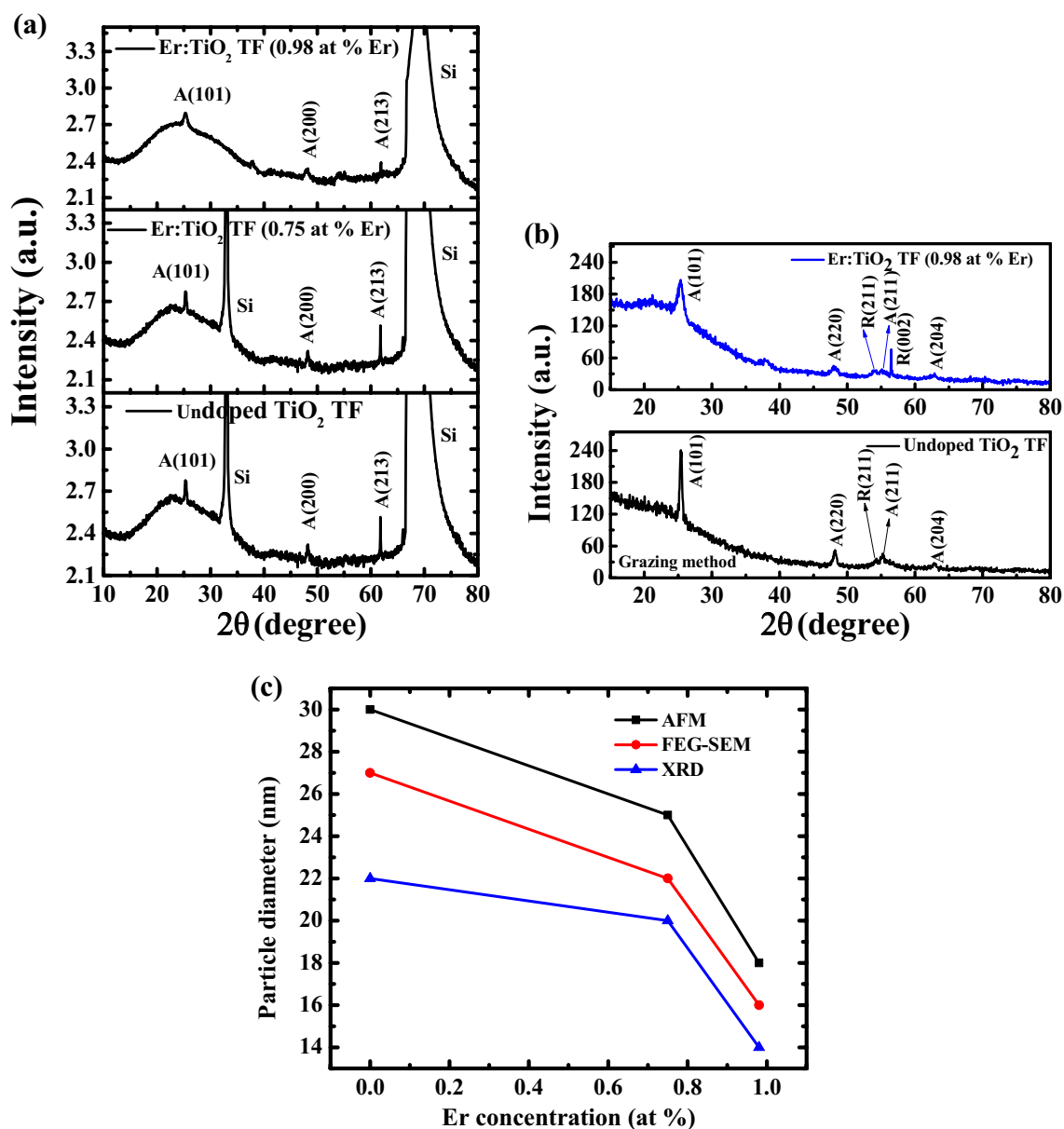
Fig. 3 **a** XRD pattern of undoped TiO$_2$ TF; Er:TiO$_2$ TF (0.75 at.% Er) and Er:TiO$_2$ TF (0.98 at.% Er) samples; **b** XRD pattern using grazing method; **c** comparison of particle size

band gap absorption, followed by relaxation and optical recombination of free electrons with trapped holes. These trapped holes could be localized at oxygen vacancies sites (V$_O$) or at Ti sites adjacent to V$_O$ [34]. On the other hand, it was shown that the red emission is related to recombination between trapped electrons and free holes [34]. The electron trap contributing to this red emission was associated to oxygen vacancies positioned below the anatase surface [34]. Both emissions quench during UV + O$_2$ exposure and are partially degraded by this treatment [34]. In fact, it was also demonstrated that the PL intensity of both emissions depends on the effect of absorption or

desorption of O$_2$. However, this change is more important for the green band. Usually, its intensity increases considerably by O$_2$ desorption. The possible mechanisms that could explain the green and red emission bands are illustrated in Fig. 5a [34]. For rutile phase, the emission band usually shows only one band at near-infrared emission (NIR) region around 830 nm. The nature of this emission is more difficult to explain. It was previously associated with a different mechanism related to optical recombination involving free holes at the valence band [34]. In fact, the NIR PL was attributed to a possible radiative recombination between mid-gap trapped electrons and free holes at
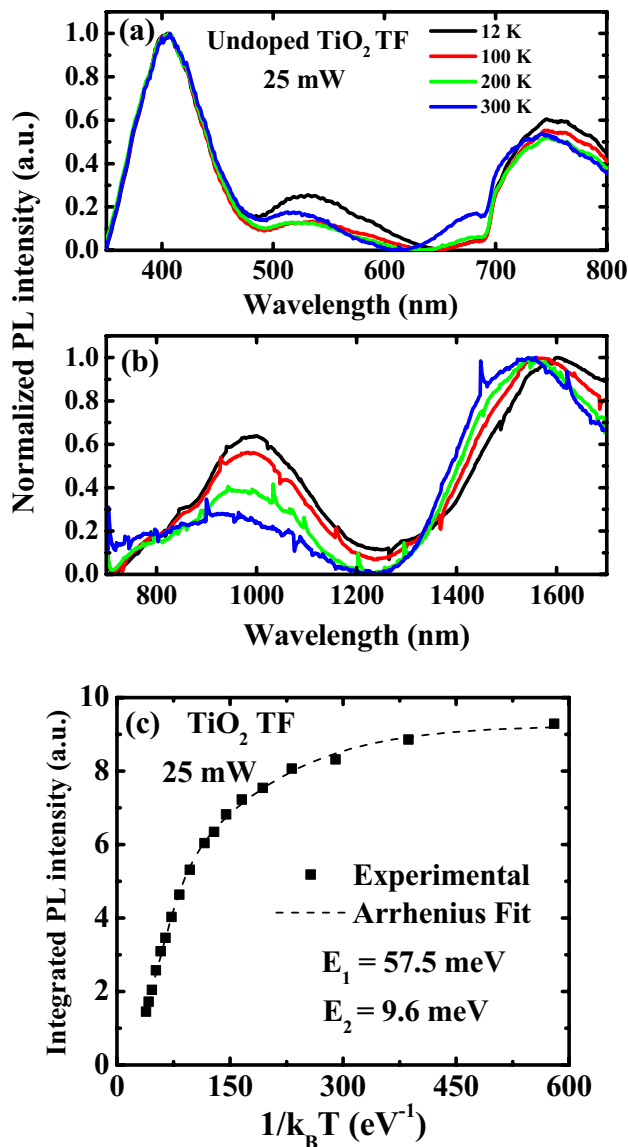
Fig. 4 Typical temperature dependence of normalized PL spectra of TiO$_2$ TF (reference sample) at 25 mW **a** visible range, **b** infrared range, **c** the Arrhenius plot for the 1000 nm band
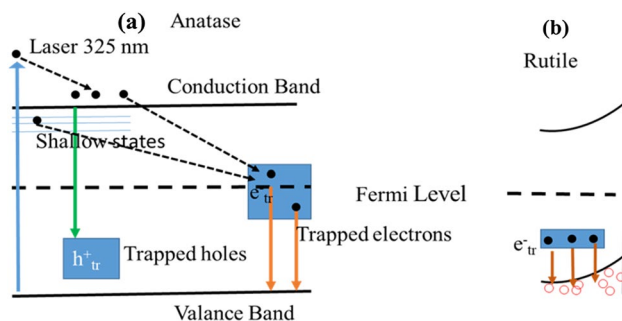

Fig. 5 **a** Possible mechanism for green and red emissions in anatase TiO$_2$ [34], **b** possible recombination for near-infrared emissions optical recombination in rutile TiO$_2$ [34]

the valence band. Figure 5b illustrates the typical optical transitions for rutile TiO$_2$.

The blue band observed in reference sample around 403 nm (Fig. 4a) was previously reported and associated with the possible contribution of rutile phase (dipole-forbidden direct transition) usually observed in crystals around 3.03 eV [35] or to the band tail emission of the anatase TiO$_2$ [18]. We remark that this band does not present important changes with the temperature. As mentioned previously the anatase phase is the dominant phase confirmed by XRD measurements. Therefore, this blue emission was mainly associated with band tail emission in the anatase phase. As stated above we have also observed a very broad band around 530 nm. This broad band seems to be a combination of two bands previously reported in the literature for the anatase phase: a green band (~ 520 nm) and a red band (~ 620 nm) [34]. However, we have observed that the intensity of the green emission dominates. Its total intensity decreases, and its peak energy presents a small blue shift with the increase of the temperature (from 530 to 515 nm, 68 meV). This band seems to have two unresolved bands: green and red emissions. We attribute this broad band to different recombination processes: (1) band gap absorption, followed by relaxation and optical recombination with trapped holes (contribution of the green band) and (2) recombination between trapped electrons and holes (contribution of the red emission). The emission around 750 nm (NIR) was previously observed only for the rutile phase and associated with the Ti^{3+} ions [37]. The rutile phase which was detected by XRD measurements using grazing method could explain our PL results in the infrared region. A possible local annealing by the UV laser could also enhance the rutile phase contribution. Actually, laser induced phase transition from anatase to rutile was previously reported [38]. As the rutile phase was detected by XRD we mainly attributed this result to the presence of the rutile phase in our samples.

In addition, two other broad peaks were also observed in the infrared region around 1000 nm and 1600 nm. There are no previous reports for the observation of these bands in TiO$_2$. Actually, all previous studies of PL of TiO$_2$ are usually performed in the spectral region of 300–900 nm. Therefore these infrared emissions have not been previously reported in the literature yet. We associated them with the rutile phase. In order to investigate in more detail the infrared emission, we have fitted the temperature dependence of the PL intensity of the 1000 nm band by:

$$I = \frac{I_0}{1 + A_1 \exp\left[\frac{-E_1}{k_B T}\right] + A_2 \exp\left[\frac{-E_2}{k_B T}\right]} \quad (2)$$

where I$_0$ = PL intensity at 0 K, E$_1$ and E$_2$ are activation energies, A$_1$ and A$_2$ are temperature independent constants, and

k_B = Boltzmann constant. Using Eq. (2), activation energies E_1 = 57.5 meV and E_2 = 9.6 meV were obtained. This emission may be associated with possible trapped electrons contribution of rutile phase as illustrated in Fig. 5b. Therefore, our results evidence the presence of two crystal phases, anatase and rutile phases: the visible PL emission is due to anatase phase in the TiO_2 host lattice, showing PL bands in the visible region around 403 and 530 nm, while the rutile phase is related to the PL bands in the infrared region around 750, 1000 and 1600 nm.

Figure 6a shows the PL spectra of Er-doped samples for different Er^{3+} concentrations at room temperature. In addition to the broad bands, several sharp intense PL bands associated to optical transitions of Er^{3+} ions are observed for both samples. Particularly, these sharp peaks are more important for the highly Er-doped TiO_2 (0.98 at.% Er) samples. It is well known that the Er-related emissions occur by indirect excitation of the Er^{3+} ions. The Er^{3+} ions are particularly excited by energy transfer of electron–hole pairs which are optically generated in the TiO_2 host. The observed emission lines are assigned to the intra-4f transitions in the Er^{3+} ions. Similarly, PL peaks observed at 525 nm, 565 nm, and 667 nm were previously observed for Er^{3+}-doped TiO_2 grown on Si substrates [18] and were associated with the transitions from the excited states ($^2H_{11/2}$, $^4S_{3/2}$ and $^4F_{9/2}$) to the ground state ($^4I_{15/2}$) of the Er^{3+} ions. The intensity of these sharp peaks presents a decrease of PL intensity at low temperature (Fig. 6b). Similar behavior was observed previously [18]. In addition, the Er^{3+} PL emission is stable, and no sample degradation was observed under UV excitation. The spectra in Fig. 6 has been normalized by taking the maximum of the emission observed at around 403 nm.

We have also investigated the PL spectra in the infrared region. Figure 7 shows the PL spectra at 12 K for undoped
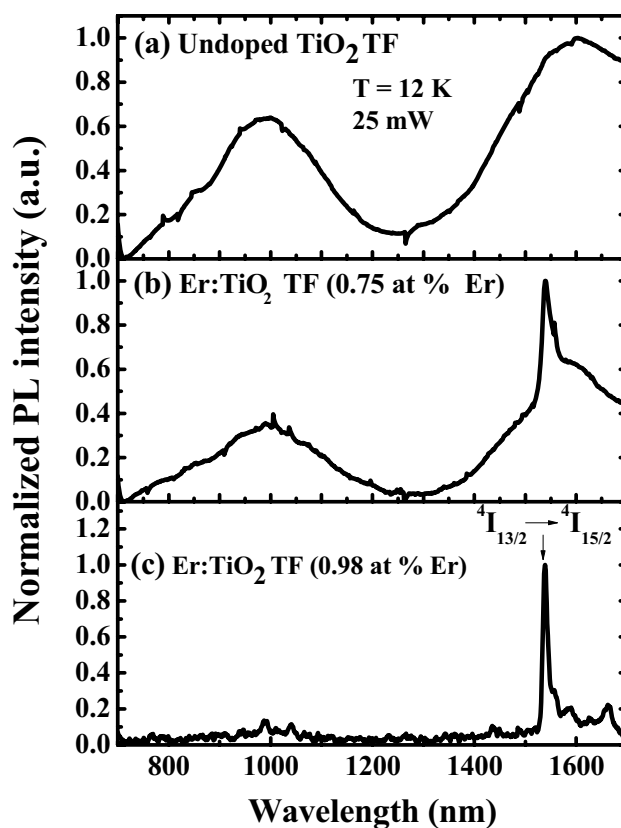

Fig. 7 Normalized PL spectra at 12 K for undoped and Er-doped TiO_2 TFs

and Er^{3+}-doped TiO_2 samples. As mentioned before the energy levels of Er^{3+} are only slightly affected by the host because the 4f electrons, which are responsible for the luminescence around 1540 nm and the up-conversion properties, are shielded by the outer 5s and 5p electrons [39].

Fig. 6 a Normalized PL spectra at 300 K for undoped TiO_2 (reference sample), and Er^{3+}-doped TiO_2 TFs with different Er concentrations. b PL spectra at 300 K and 12 K for Er-doped TiO_2 (0.98 at.% Er) TF
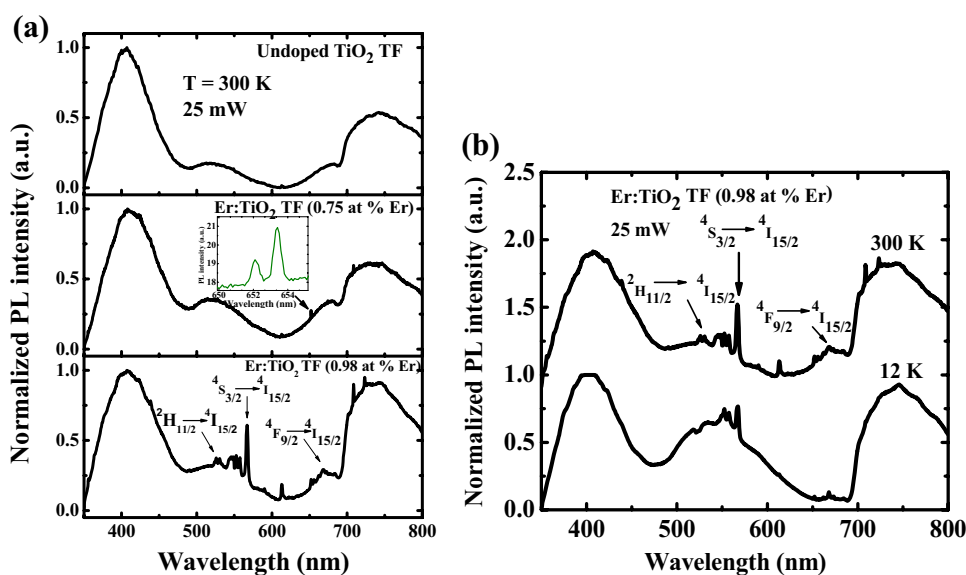
Therefore, the interaction between the local electric field of the TiO_2 host and the $4f$ electrons would be weak. As a result, the local host structure around Er^{3+} would only result in the minor splitting of the free-ion energy levels, $^{2S+1}L_J$, into multiplets. This splitting is usually called CF splitting or Stark splitting, and the number of CF sublevels is determined by the symmetry of the surrounding crystal host, such that a reduction in the symmetry around the lanthanide ions will introduce a higher number of sub-levels. It was previously observed that the crystallinity of TiO_2 affects considerably the light emission from Er^{3+}, and the CF splitting of the energy levels of Er^{3+}. In the polycrystalline TiO_2

TF, light emission from two different Er^{3+} environments was observed. These effects were associated with Er^{3+} ions populating the dominant anatase phase or rutile environment which results in some different light emission behavior [39].

It was also observed that at higher Er^{3+} concentration the broad bands are suppressed and emissions from Er^{3+} ions are the main contribution for the PL spectrum (Fig. 7c). The emission associated with $^4I_{13/2} \rightarrow {}^4I_{15/2}$ transition in Er^{3+} ions is observed at around 1.54 μm and can be observed at room temperature (Fig. 8), where the spectra were normalized by taking the maximum of this emission. As the temperature was decreased to 12 K, the main peak position at 1.54 μm did not present important changes. Actually, this Er-related emission is nearly independent of the host and temperature because of the screening of the unfilled inner $4f^{11}$ shell by the outer closed $5s^25p^6$ shells [40]. However, the FWHM decreases from 4.97 to 3.4 meV. In addition, more peaks can be observed at 300 K and the PL intensity at 1.537 μm of the Er-doped TiO_2 TF (0.98 at.% Er) increases to about four times with decrease in temperature to 12 K. Similar behavior of increase in PL intensity at lower temperatures was observed previously [18]. The inset of Fig. 8 shows the temperature dependence of PL intensity of sharp peaks in the infrared region. In conclusion, Er^{3+} doped TiO_2 TFs exhibit broad and sharp emissions. The broad emissions are due to the TiO_2 host and sharp peaks are associated with optical transitions in Er^{3+} ions. The PL peaks in the infrared region (900–1700 nm) are observed here for the first time in TiO_2 reference samples and are associated with rutile phase. A strong emission near infrared region due to Er^{3+} was detected at 1.54 μm. In addition, it was observed that broad bands in infrared region are suppressed with the incorporation of Er^{3+} due to the energy transfer from the TiO_2 host to Er^{3+} ions.
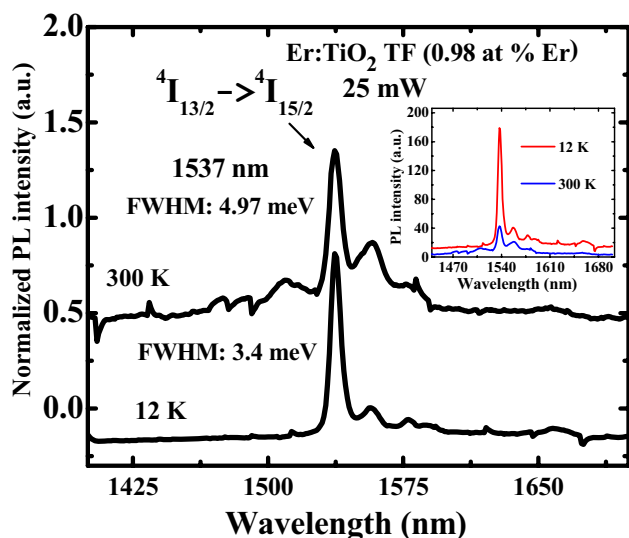

Fig. 8 Normalized PL spectra for Er-doped TiO_2 TF (0.98 at.% Er) sample at 300 K and 12 K in the infrared region. Temperature dependence of PL intensity of sharp peaks (inset)

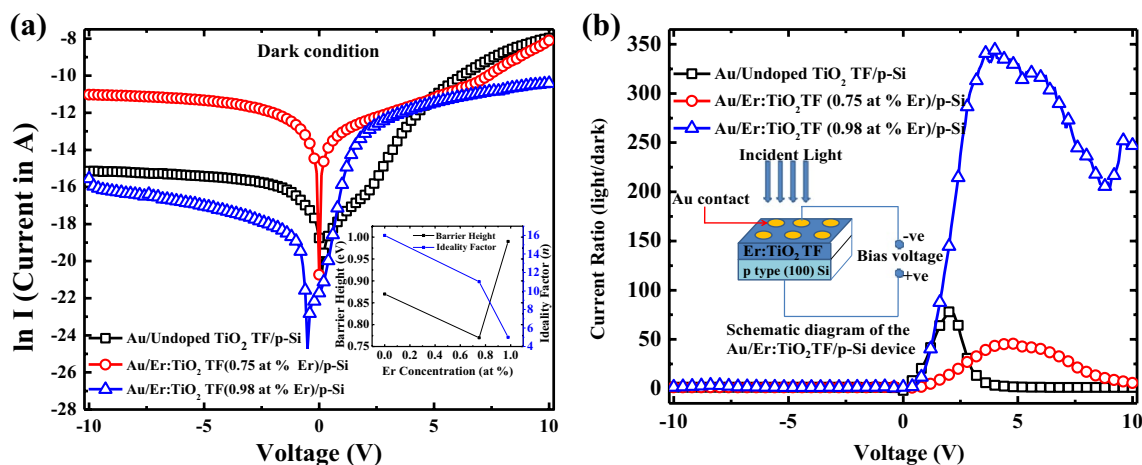**Fig. 9 a** ln I–V characteristics of the devices. The inset shows the variation of ideality factor and barrier height of the devices as a function of doping concentration. **b** Current ratio (light/dark) versus voltage of the undoped and doped TF based devices. The inset shows a schematic diagram of the devices

3.4 Current–voltage (I–V) characteristics

Figure 9a shows the room temperature ln I–V characteristics of Au/TiO$_2$ TF/p-Si and Au/Er-doped TiO$_2$ TF/p-Si devices in dark condition. The ratio of light current to dark current versus voltage characteristics for the devices (under white light illumination using a xenon arc lamp) is shown in Fig. 9b. The ideality factor (n) and barrier height (ϕ_b) of the devices were calculated from Fig. 9a using Eqs. (3) and (4) [41].

$$n = \frac{q}{kT}\left[\frac{\partial V}{\partial(\ln I)}\right] \qquad (3)$$

$$\phi_b = \frac{kT}{q}\ln\frac{AA^*T^2}{I_0} \qquad (4)$$

where q is the charge of an electron, k is the Boltzmann constant, V is the applied voltage across the electrodes, T is the absolute temperature in Kelvin, $\frac{\partial(\ln I)}{\partial V}$ is the slope of the ln I–V curve (taken between 0.2 and 1 V), A is the surface area of a single Au dot, A* (671 A/cm^2/K^2) [42] is the effective Richardson constant of TiO$_2$ and I_0 is the reverse saturation current given by Eq. (5).

$$I_0 = AA^*T^2e^{(-q\phi_b/kT)} \qquad (5)$$

From the intercept of the linear fit (between 0.2 and 1 V) of the dark ln I–V plot, I_0 is found to be equal to 1.38×10^{-9} A, 5.10×10^{-8} A and to 2.53×10^{-11} A for the undoped TiO$_2$ TF, Er-doped TiO$_2$ (0.75 at.% Er), and Er-doped TiO$_2$ (0.98 at.% Er), respectively. I_0 first increases then decreases as the Er doping increases. The ϕ_b and n for the undoped TiO$_2$ TF are ~0.87 eV and ~16, respectively. The high value of n suggests

the presence of large number of defects in the metal/semiconductor interface. First, the barrier height decreases to ~0.77 eV for Er-doped TiO$_2$ TF (0.75 at.% Er) and then increases to ~0.99 eV for the higher Er-doped sample (0.98 at.% Er). The value of n gradually decreases to ~11 and ~5 with increasing Er^{3+} concentration as shown in Fig. 9a (inset). The gradual decrease in n value indicates the better diode performance with the increase of Er^{3+} doping, which may be due to simultaneous removal of the oxygen related defects as observed in Er^{3+} doped In$_2$O$_3$ material [31]. The barrier heights of 0.77–0.99 eV deduced from I–V characteristics using the classical thermionic emission theory are in good agreement with other reported values [43]. There was a decrease in barrier height due to the role of the electron affinity (~4 eV for TiO$_2$) in the band bending formation [44]. With high Er^{3+} doping concentration, those oxygen related defects were mostly neutralized and it results in the non-availability of excessive free electrons and subsequently there was a reduction in I_0 value. The barrier height then increases more to match the new band alignment with gold (work function ~4.9 eV) [43].

3.5 Responsivity, internal gain and temporal response

The suitability of devices as optical detectors is verified by measuring the responsivity and temporal response, which are shown in Fig. 10. The responsivity (R) of the devices at room temperature was calculated at different wavelengths under the applied bias voltage of 2 V using Eq. (6) and is shown in Fig. 10a.
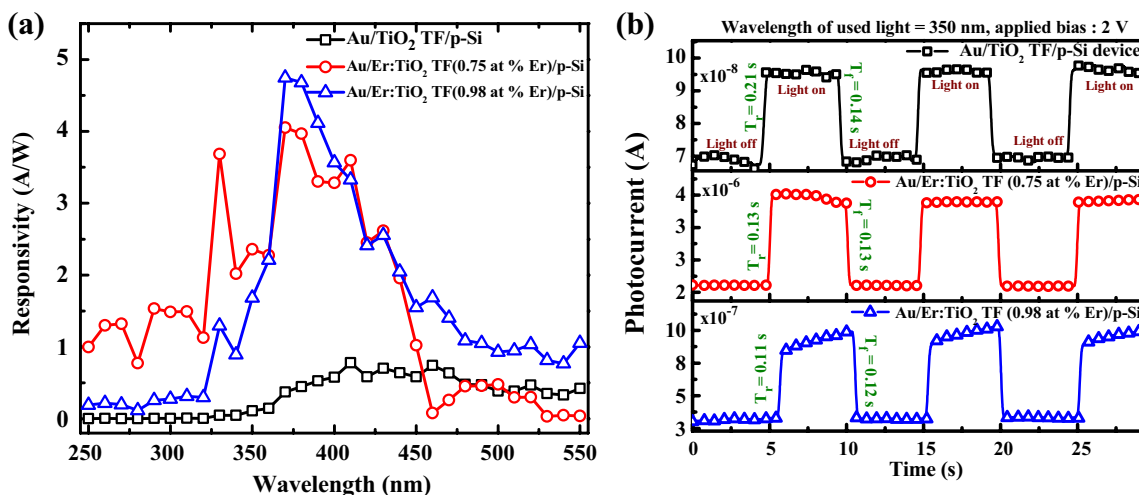
$$R = \frac{I_{photo}}{P_{opto}} \qquad (6)$$

Fig. 10 **a** Responsivity versus wavelength curves of the devices, **b** temporal responses of the devices with the illumination of 350 nm wavelength of light

where I_{photo} is the photocurrent and P_{opto} is the optical power.

The responsivity of the highest doped TiO_2 TF device is bigger than that of the undoped TiO_2 TF over the wavelength range 250–550 nm (Fig. 10a). The highest doped device showed maximum responsivity at 370 nm, which is ~13 times higher than the undoped device (Fig. 10a). The corresponding photon energy ~3.35 eV of the Er-doped TiO_2 material can be attributed to the near band edge absorption of light as TiO_2 material is only active to UV light of energy > 3.0 eV [45]. In forward bias, a large number of photo-generated electron–hole pair increases the majority carrier and ionizes the interface states. The ionization of interface states increases the barrier height, but the large number of electrons, generated upon UV illumination, effectively reduces the barrier height under forward bias resulting in band bending changes and current increases. Again the doping of TiO_2 with Er^{3+} ions efficiently traps the photo generated electrons, which prevent the electron–hole recombination process resulting in an enhancement of the photo responsivity of the detector [46].

However, there was no significant responsivity recorded for the undoped TiO_2 material. A broad peak in the visible region of light around 425 nm was observed, which may be due to the release of trapped electron–holes at oxygen vacancies in the undoped TiO_2 material [47]. The maximum internal gain (G) of ~15 was calculated at a wavelength of 370 nm by using Eq. (7), which is much greater than the undoped TiO_2 TF (~1.5).

$$G = \frac{Rhc}{\lambda q \eta} \qquad (7)$$

where h is the Planck's constant, c is the speed of light, λ is the wavelength of incident radiation, q is the electronic charge, and η is the quantum efficiency (assuming $\eta = 1$).

The temporal response of undoped and Er-doped TiO_2 TFs under illumination of 350 nm wavelength of light at an applied bias of 2 V is shown in Fig. 10b. The rise time (T_r) and fall time (T_f) of the devices were obtained by considering the time required by the pulse to increase from 10 to 90% of its peak value and the time required by the pulse to decrease from 90% of the peak value to 10%, respectively. The undoped TiO_2 shows $T_r \sim 0.21$ s and $T_f \sim 0.14$ s. Those values showed a continuous improvement in switching behavior and calculated values were $T_r \sim 0.13$ s, $T_f \sim 0.13$ s and $T_r \sim 0.11$ s, $T_f \sim 0.12$ s for lowest and highest doped devices, respectively. The current value rises slowly from a minimum to a maximum value for the highest doped device under light on condition due to the diffusion of charge carriers for a longer time [32]. However, the drift velocity of the carriers is larger than diffusion velocity. Thus, ultimately the photo generated carriers drift faster and reduce T_r and T_f for the highest Er-doped photodetector. In the case of the undoped TiO_2 device, the depletion width is less under

reverse bias (as holes are trapped in oxygen defects), which results in absorption of incident photons in the diffusion region. Therefore, the temporal response of the undoped device is affected by diffusion carriers and makes it unreliable in light on condition. The device shows improved performance with more Er^{3+} doping into TiO_2 sample by enlarging the depletion region at the metal/semiconductor junction and by reducing the oxygen defects. As the incident photons are mostly absorbed in the depletion region, this results in the generation of drift carriers and a reduction in the effect of diffusion on the temporal response of the device. A similar effect was also described by Ghosh et al. [31]. From the above experiment, it can be concluded that the Er^{3+} doped detector possesses reliable photo-switching characteristics at the particular wavelength of 350 nm and applied voltage of 2 V.

4 Conclusions

In conclusion, we have synthesized Er^{3+}-doped TiO_2 TFs using sol–gel synthesis method. The XRD spectra revealed the presence of various planes of body-centered tetragonal anatase phase of TiO_2 and small contribution of rutile phase. An increase in the concentration of Er^{3+} ions resulted in a decrease of the crystallite size. The average particle sizes calculated from FEG–SEM images were ~27 nm, 22 nm and 16 nm for undoped TiO_2 TF, 0.75 at.% Er doped TiO_2 TF and 0.98 at.% Er-doped TiO_2 TF respectively which is analogous the particle size estimated from AFM and XRD analysis. From temperature dependent PL spectra of undoped TiO_2 TF, broad bands in visible and infrared region were detected. The emissions in visible region were associated with the dominant anatase phase and in the infrared region with the rutile phase. Particularly we report for the first time PL bands for TiO_2 in the region of 800–1700 nm. For Er^{3+} doped TiO_2 samples, the PL peaks observed at 525, 565, and 667 nm were associated with the transitions from the excited states ($^2H_{11/2}$, $^4S_{3/2}$ and $^4F_{9/2}$) to the ground state ($^4I_{15/2}$) of the Er^{3+} ions. At higher Er^{3+} concentration, the emission from $^4I_{13/2} \rightarrow {}^4I_{15/2}$ transition in Er^{3+} ions was prominent at around 1.54 μm. The PL intensity at 1.537 μm of the Er-doped TiO_2 TF (0.98 at.% Er) increased to about four times with decrease in temperature down to 12 K. From I–V characteristics of the doped and undoped devices, the barrier height of the undoped TiO_2 TF was calculated to be ~0.87 eV which decreases to ~0.77 eV for moderately Er-doped TiO_2 TF (0.75 at.% Er) and increased to ~0.99 eV for higher Er-doped TiO_2 (0.98 at.% Er). With an increase in Er doping, there was a gradual decrease in ideality factor as well as the reverse saturation current due to simultaneous removal of the oxygen related

defects. At 370 nm, the Er-doped TiO_2 TF (0.98 at.% Er) based devices showed ~ 13 times enhanced responsivity as compared to the undoped device. The Er-doped TiO_2 TF (0.98 at.% Er) based devices exhibited a maximum internal gain (G) of ~ 15 at a wavelength of 370 nm. From the temporal response, the undoped TiO_2 showed rise and fall times of ~ 0.21 s and ~ 0.14 s, respectively, while for the lowest and highest doped devices parameters were ~ 0.13 s and ~ 0.13 s; ~ 0.11 s and ~ 0.12 s, respectively. This clearly indicates the enhancement in switching performance with an increase in Er doping concentration.

References

1. A. Fujishima, T.N. Rao, D.A. Tryk, J. Photochem. Photobiol. C **1**, 1–21 (2000). https://doi.org/10.1016/S1389-5567(00)00002-2
2. X. Chen, S.S. Mao, J. Chem. Rev. **107**(7), 2891–2959 (2007). https://doi.org/10.1021/cr0500535
3. A.-W. Xu, Y. Gao, H.-Q. Liu, J. Catal. **207**, 151–157 (2002). https://doi.org/10.1006/jcat.2002.3539
4. M. Ferroni, V. Guidi, G. Martinelli, G. Faglia, P. Nelli, G. Sberveglieri, Nanostruct. Mater. **7**(7), 709–718 (1996). https://doi.org/10.1016/S0965-9773(96)00050-5
5. N. Savage, B. Chwieroth, A. Ginwalla, B.R. Patton, S.A. Akbar, P.K. Dutta, Sens. Actuators B **79**, 17–27 (2001). https://doi.org/10.1016/S0925-4005(01)00843-7
6. T. Xie, A. Rani, B. Wen, A. Castillo, B. Thomson, R. Debnath, T.E. Murphy, R.D. Gomez, A. Motayed, Thin Solid Films **620**, 76–81 (2016). https://doi.org/10.1016/j.tsf.2016.07.075
7. M. Selman, Z. Hassan, Sens. Actuators A **221**, 15–21 (2015). https://doi.org/10.1016/j.sna.2014.10.041
8. F. Li, Y. Gu, Mater. Sci. Semicond. Process. **15**, 11–14 (2012). https://doi.org/10.1016/j.mssp.2011.04.008
9. Y.Y. Hui, P.H. Shih, K.J. Sun, C.F. Lin, Thin Solid Films **515**, 6754–6757 (2007). https://doi.org/10.1016/j.tsf.2007.02.013
10. D.S. Lee, A.J. Steckl, Appl. Phys. Lett. **80**, 1888–1890 (2002). https://doi.org/10.1063/1.1461884
11. L. Yang, T. Carmon, B. Min, S.M. Spillane, K.J. Vahala, Appl. Phys. Lett. **86**, 091114 (2005). https://doi.org/10.1063/1.1873043
12. S.G. Krishnan, P.S. Archana, B. Vidyadharan, I.I. Misnon, B.L. Vijayan, V.M. Nair, A. Gupta, R. Jose, J. Alloys Compd. **684**, 328–334 (2016). https://doi.org/10.1016/j.jallcom.2016.05.183
13. A. Ganguly, A. Mondal, B. Choudhuri, T. Goswami, K.K. Chattopadhyay, J. Adv. Sci. Eng. Med. **6**, 797–801 (2014). https://doi.org/10.1166/asem.2014.1566
14. H. Ishiguro, R. Nakano, Y. Yao, J. Kajioka, A. Fujishima, K. Sunada, M. Minoshima, K. Hashimoto, Y. Kubota, J. Photochem. Photobiol. Sci. **10**, 1825–1829 (2011). https://doi.org/10.1039/c1pp05192j
15. J. Reszczyn´ska, T. Grzyb, J.W. Sobczak, W. Lisowski, M. Gazda, B. Ohtani, A. Zaleska, Appl. Surf. Sci. **307**, 333–345 (2014). https://doi.org/10.1016/j.apsusc.2014.03.199
16. T.K. Srinivasan, B.S. Panigrahi, N. Suriyamurthy, P.K. Parida, B. Venkatraman, J. Rare Earths **33**(1), 20 (2015). https://doi.org/10.1016/S1002-0721(14)60377-X
17. G. Xing, Z. Zhang. S. Qi, G. Zhou, K. Zhang, Z. Cui, Y. Feng, Z. Shan, S. Meng, Opt. Mater. **75**, 102–108 (2018). https://doi.org/10.1016/j.optmat.2017.10.006
18. S. Kumoro, T. Katsumata, H. Kokai, T.M.X. Zhao, Appl. Phys. Lett. **81**(25), 4733–4735 (2002). https://doi.org/10.1063/1.1530733
19. L. Skowronski, R. Szczesny, K. Zdunek, Thin Solid Films **632**, 112–118 (2017). https://doi.org/10.1016/j.tsf.2017.04.041
20. S. Wang, G. Xia, H. He, K. Yi, J. Shao, Z. Fan, J. Alloys Compd. **431**, 287–291 (2007). https://doi.org/10.1016/j.jallcom.2006.05.091
21. M. Ueda, Y. Uchibayashi, S. Otsuka-Yao-Matsuo, T. Okura, J. Alloys Compd. **459**, 369–376 (2008). https://doi.org/10.1016/j.jallcom.2007.04.266
22. D.S. Gospodinova, L.P.H. Jeurgens, U. Welzel, L. Bauermann, R.C. Hoffmann, J. Bill, Thin Solid Films **520**, 5928–5935 (2012). https://doi.org/10.1016/j.tsf.2012.03.047
23. H.-Y. Liu, W.-H. Lin, W.-C. Sun, S.-Y. Wei, S.-M. Wu, Mater. Sci. Semicond. Process. **57**, 90–94 (2017). https://doi.org/10.1016/j.mssp.2016.10.005
24. T. Watanabe, S. Fukayama, M. Miyauchi, A. Fujishima, K. Hashimoto, J. Sol-Gel Sci. Technol. **19**, 71–76 (2000). https://doi.org/10.1023/A:1008762121743
25. J. Xing, H. Wei, E.-J. Guo, F. Yang, J. Phys. D **44**, 375104 (2011). https://doi.org/10.1088/0022-3727/44/37/375104
26. K. Lv, M. Zhang, C. Liu, G. Liu, H. Li, S. Wen, Y. Chen, S. Ruan, J. Alloys Compd. **580**, 614–617 (2013). https://doi.org/10.1016/j.jallcom.2013.07.161
27. D.B. Patel, K.R. Chauhan, S.-H. Park, J. Kim, Mater. Sci. Semicond. Process. **64**, 137–142 (2017). https://doi.org/10.1016/j.mssp.2017.03.024
28. W.F. Xiang, P.R. Yang, A.J. Wang, K. Zhao, H. Ni, S.X. Zhong, Thin Solid Films **520**, 7144–7146 (2012). https://doi.org/10.1016/j.tsf.2012.07.110
29. M. Zhang, D. Li, J. Zhou, W. Chen, S. Ruan, J. Alloys Compd. **618**, 233–235 (2015). https://doi.org/10.1016/j.jallcom.2014.07.040
30. L. Miao, X. Xiao, F. Ran, S. Tanemura, G. Xu, Jpn. J. Appl. Phys. **50**, 061101 (2011). https://doi.org/10.1143/JJAP.50.061101
31. A. Ghosh, A. Mondal, A. Das, S. Chattopadhyay, K.K. Chattopadhyay, J. Alloys Compd. **695**, 1260–1265 (2017). https://doi.org/10.1016/j.jallcom.2016.10.254
32. R. Lahiri, A. Ghosh, S.M.M. Dhar Dwivedi, S. Chakrabartty, P. Chinnamuthu, A. Mondal, Appl. Phys. A **123**, 573 (2017). https://doi.org/10.1007/s00339-017-1180-2
33. D.Y. Lee, J.-T. Kim, J.-H. Park, Y.-H. Kim, I.-K. Lee, M.-H. Lee, B.-Y. Kim, Curr. Appl. Phys. **13**, 1301–1305 (2013). https://doi.org/10.1016/j.cap.2013.03.025
34. D.K. Pallotti, L. Passoni, P. Maddalena, F. Di Fonzo, S. Lettieri, J. Phys. Chem. C **121**, 9011–9021 (2017). https://doi.org/10.1021/acs.jpcc.7b00321
35. H. Tang, K. Prasad, R. Sanjinès, P.E. Schmid, F. Lévy, J. Appl. Phys. **75**(4), 2042–2047 (1994). https://doi.org/10.1063/1.356306
36. W. Luo, C. Fu, R. Li, Y. Liu, H. Zhu, X. Chen, Small **7**(21), 3046–3056 (2011). https://doi.org/10.1002/smll.201100838
37. Y. Yang, C. Wang, L. Xiang, X. Ma, D. Yang, AIP Adv. **4**, 047109 (2014). https://doi.org/10.1063/1.4871188
38. G.C. Vásquez, M.A. P-Herrero, D. Maestre, A. Gianoncelli, J. R-Castellanos, A. Cremades, J. G-Calbet, J. Piqueras, J. Phys.

Chem. C **119**(21), 11965–11974 (2015). https://doi.org/10.1021/acs.jpcc.5b01736

39. S.R. Johannsen, S. Roesgaard, B. Julsgaard, R.A.S. Ferreira, J. Chevallier, P. Balling, S.K. Ram, A.N. Larsen, Opt. Mater. Express **6**(5), 1664–1678 (2016). https://doi.org/10.1364/OME.6.001664

40. M. Jiang, C. Zhu, J. Zhou, J. Chen, Y. Gao, X. Ma, D. Yang, J. Appl. Phys. **120**, 163104 (2016). https://doi.org/10.1063/1.4966224

41. A. Mondal, A. Ganguly, A. Das, B. Choudhuri, R.K. Yadav, Plasmonic **10**(3), 667–673 (2015). https://doi.org/10.1007/s11468-014-9852-7

42. P.B. Pillai, A.N. Corpus Mendoza, M.M. De Souza, G. Bree, D. Jeng, J. Renew. Sustain. Energy **6**, 013142 (2014). https://doi.org/10.1063/1.4866260

43. N. Szydlo, R. Poirier, J. Appl. Phys. **51**, 3310 (1980). https://doi.org/10.1063/1.328037

44. J.G. Mavroides, D.I. Tchernev, J.A. Kafalas, D.F. Kolesar, Mater. Res. Bull. **10**, 1023–1030 (1975). https://doi.org/10.1016/0025-5408(75)90210-X

45. T. Umebayashi, T. Yamaki, H. Itoh, K. Asai, Appl. Phys. Lett. **81**(3), 454–456 (2002). https://doi.org/10.1063/1.1493647

46. S.N. Das, K.-J. Moon, J.P. Kar, J.-H. Choi, J. Xiong, T. Lee, J.-M. Myoung, Appl. Phys. Lett. **97**, 022103-1–022103-3 (2010). https://doi.org/10.1063/1.3464287

47. P. Chinnamuthu, J.C. Dhar, A. Mondal, A. Bhattacharyya, N.K. Singh, J. Phys. D **45**, 135102 (2012). https://doi.org/10.1088/0022-3727/45/13/135102